## **PAPER**

# Maximizing the rate sensitivity of resonating gyroscopes using nonlinear shape optimization

To cite this article: Pavel M Polunin and Steven W Shaw 2022 J. Micromech. Microeng. 32 064003

View the article online for updates and enhancements.

# You may also like

- A MEMS gyroscope high-order calibration method for highly dynamic environments Jinwen Wang, Zhihong Deng, Xinyu Liang et al
- Analysis of compensation for a qsensitivity scale-factor error for a MEMS vibratory gyroscope
   Byung Su Park, KyungJun Han, SangWoo
- The Gravity Probe B test of general relativity

C W F Everitt, B Muhlfelder, D B DeBra et



# ECS Membership = Connection

# ECS membership connects you to the electrochemical community:

- Facilitate your research and discovery through ECS meetings which convene scientists from around the world;
- Access professional support through your lifetime career:
- $\bullet$  Open up mentorship opportunities across the stages of your career;
- Build relationships that nurture partnership, teamwork—and success!

Join ECS! V

Visit electrochem.org/join



J. Micromech. Microeng. 32 (2022) 064003 (13pp)

https://doi.org/10.1088/1361-6439/ac6c74

# Maximizing the rate sensitivity of resonating gyroscopes using nonlinear shape optimization

# Pavel M Polunin<sup>1,2,3,\*</sup> and Steven W Shaw<sup>1,2,4</sup>

- <sup>1</sup> Department of Mechanical Engineering, Michigan State University, East Lansing, MI 48823, United States of America
- <sup>2</sup> Department of Physics and Astronomy, Michigan State University, East Lansing, MI 48823, United States of America
- <sup>3</sup> SiTime Corporation, Santa Clara, CA 95054, United States of America
- <sup>4</sup> Department of Mechanical and Civil Engineering, Florida Institute of Technology, Melbourne, FL 32901, United States of America

E-mail: poluninp@msu.edu

Received 5 December 2021, revised 27 April 2022 Accepted for publication 3 May 2022 Published 13 May 2022



### **Abstract**

In this work we demonstrate how one can improve the angular rate sensitivity of ring/disk resonating gyroscopes by tailoring their nonlinear behavior by systematic shaping of the gyroscope body and electrodes, and by the tuning of bias voltages on segmented electrodes. Of specific interest are the drive and sense mode Duffing nonlinearities, which limit their dynamic ranges, and the intermodal dispersive coupling between these modes that provides parametric amplification of the sense mode output signal. These two effects have the same physical origins and are in competition in terms of system performance, which naturally calls for optimization considerations. The present analysis is based on a systematic modeling of the nonlinear response of these devices by which we explore ways in which one can optimize the angular rate sensitivity by manipulating the mechanical and electrostatic contributions to the nonlinearities. In particular, non-uniform modifications of the gyroscope body thickness are employed to affect the mechanical contributions to these parameters, while the electrostatic components are manipulated via shaping of the resonator-electrode gap and by applying non-uniform bias voltages among segmented electrodes around the gyroscope body. These models predict that such relatively simple alterations can achieve improvements in gain by about an order of magnitude when compared to devices with uniform layouts.

Keywords: MEMS rate gyroscope, gyroscope sensitivity, self-induced parametric amplification, Duffing nonlinearity, modal coupling, shape optimization

(Some figures may appear in colour only in the online journal)

# 1. Introduction

Micro-electromechanical (MEMS) vibratory gyroscopes are appealing due to their size, high quality factors, low power consumption, and compatibility with integrated circuits [1],

\* Author to whom any correspondence should be addressed.

which make them favored in smartphone applications [2, 3], electronic stability control systems for automotive safety [4, 5], robotics [6], medical diagnostics [7], and military applications [8]. This demand motivates an ongoing drive for increased precision and lower cost. Here we describe how one can make use of and optimize the intermodal parametric pumping of the sense mode by the drive mode, as reported in [9], and thereby significantly increase gyroscope

sensitivity to an external angular rate. The approach is based on the systematic nonlinear modeling of vibratory gyroscopes described in [10].

Vibratory gyroscopes operate using the Coriolis effect, which acts on objects that are moving radially in a rotating reference frame. MEMS vibratory gyroscopes are generally based on a micromechanical resonator that possesses two vibration modes with equal frequencies, one of which, the drive mode, is driven into resonance using an external periodic forcing or in a self-sustained oscillator [11]. In the presence of an external angular velocity  $\Omega$ , the Coriolis effect couples the two modes, resulting in a resonant response in the sense mode. When  $\Omega$  is much less than the gyroscope eigenfrequenices, and the modes are operating in their linear range, the sense mode amplitude is proportional to  $\Omega$  and the external angular rate can thus be estimated.

Good sensitivity to small angular rates is one of the most important characteristics of modern MEMS gyroscopes. In order to achieve high rate sensitivity one generally has to solve multiple challenging problems, including matching the frequencies of the drive and sense modes in degeneratemode gyroscopes [12–14], compensating the quadrature error between the gyroscopic modes [15–17], and maximizing modal quality factors, for example, by optimizing the geometry of the resonator body [18, 19]. As a result, ring and disk resonating gyroscopes are frequently chosen as ideal candidates for degenerate-mode vibratory gyroscopes because of the inherent symmetry of their flexural modes [15, 20-23]. However, until recently, most of the aforementioned methods and techniques were designed and implemented in MEMS gyroscopes that operated in the linear resonant regime for both vibratory modes.

Nonlinear operation of vibratory MEMS gyroscopes has been receiving an increasing attention during the past decade. In particular, the problem of improving the sensitivity of rate gyroscopes by using parametric actuation [24-27] and combined schemes of direct and parametric excitation [28, 29] have been studied both theoretically and experimentally. It has also been shown that nonlinear operation can be beneficial to the performance of MEMS gyroscopes due to the wide frequency range of the nonlinear resonant response [30]. Additionally, there has been progress in the tuning of individual modal Duffing nonlinearities in a MEMS rate gyroscope, to extend its linear dynamic range, by modifying the shape of comb drive fingers [31]. The problem of tailoring nonlinear response in coupled-mode systems by shape design has been addressed very recently [32] but remains largely unexplored, particularly for MEMS gyroscopes.

Recent experimental results demonstrated a substantial increase in the rate sensitivity in a MEMS disk resonating gyroscope when the drive mode operates in a nonlinear regime [9]. In that work, the authors hypothesized that the observed increase of the gyroscopic rate sensitivity is caused by a parametric amplification of the sense mode arising from nonlinear elastic coupling between the drive and sense modes. It is important to note that this additional gain comes with no additional complications, other than those related to the nonlinear response. More recently, the hypothesis of this self-induced

parametric amplification has been confirmed by the detailed modeling and analysis of the nonlinear vibrations of circular disk and ring rotating elastic structures in the presence of electrostatic actuation/sensing schemes [10]. In particular, it was shown that nonlinear dispersive modal coupling<sup>5</sup> arises naturally in ring/disk resonating gyroscopes due to nonlinear mechanical and electrostatic effects. The strength of this coupling is described in the present model by a coefficient  $\kappa$ . Due to the degeneracy of the gyroscope drive and sense modes, it was shown that the drive mode parametrically pumps the sense mode with a strength  $\propto |\kappa| a^2$ , where a is the non-dimensional amplitude of the drive mode response. As a result, in order to improve the gyroscope performance as a rate sensor, it is desirable to increase the strength of the dispersive modal coupling  $|\kappa|$  and/or the drive mode amplitude a. Since it is preferential to operate the gyroscope in its linear range, the maximum achievable amplitude a is limited by the Duffing nonlinearity of the drive mode, which is described in the present model by a coefficient  $\gamma$ . It is important to note that design changes alter both of these coefficients in a coupled manner, and thus their combined effects, and their tuning by design, must be considered using a physics based model. Therefore, the problem of maximizing gyroscope sensitivity requires a systematic study of nonlinear input/output characteristics of this coupled mode system, as derived in [10].

In this work we examine ways in which one can use simple design alterations to systematically manipulate the mechanical and/or electrostatic contributions to the aforementioned nonlinear effects in order to improve, and even optimize, gyroscope sensitivity. The approach taken is a simplified version of the shape optimization techniques described in [32–34]. Specifically, since the devices of interest have circular symmetry and mode degeneracy must be maintained, non-uniform shapes can be easily expressed in terms of Fourier coefficients, making the approach less computationally intensive, even analytical for some geometrical modifications.

Since electrostatic effects are known to typically dominate nonlinear effects in MEMS gyroscopes, we first investigate the dependence of electrostatic contributions, described by coefficients  $\kappa_e$  for nonlinear inter-modal coupling and  $\gamma_e$  for Duffing nonlinearity, that arise from a spatially non-uniform bias voltage,  $V_{DC}(\theta)$ , and a non-uniform electrode gap size,  $\Delta(\theta)$ , which is parameterized by the circumferential angle  $\theta$ around the gyroscope body. We formulate conditions on the non-uniformity of these parameters that preserve the degeneracy of the gyroscopic modes and demonstrate how these nonuniformities can be used to modify  $\kappa_e$  and  $\gamma_e$  and their effects on the gyroscope sensitivity. Such optimization approaches are of particular interest since they do not depend on the specific geometric features of the gyroscope body. We apply this approach to a representative ring/disk resonating gyroscope and show how certain modifications of the resonator-electrode spacing and bias voltage distribution can result in an increase of up to 3-fold of the intermodal coupling strength between

<sup>&</sup>lt;sup>5</sup> This type of coupling is referred to as *dispersive* since it reflects a change in frequency of one mode due to the amplitude of vibration of another mode.

the drive and sense modes,  $\kappa_e$ , and an attendant nearly 12-fold increase of the angular rate sensitivity.

We also analyze how changes in the geometry of the resonator body that maintain the required symmetry can be used to alter the mechanical nonlinearities, expressed by coefficients  $\kappa_m$  and  $\gamma_m$ . We illustrate the applicability of this approach by its application to a thin rotating ring for which we allow the radial ring thickness to vary along  $\theta$ . The results show the possibility of altering both  $\kappa_m$  and  $\gamma_m$ , which is relevant for micromechanical gyroscopes with dominant mechanical nonlinearities. It should be noted that we consider simple design alterations that can be expressed in terms of only a few coefficients, which makes the problem analytically manageable, but further improvements can likely be achieved using more detailed, finite-element based models, as described in [32]. In fact, a recent computational study shows that the two-mode model employed herein matches results obtained for the nonlinear dynamics of a detailed finite element model of the system, including extraneous modes, such as translational, rotational and out-of-plane eigenmodes, [35]. Furthermore, such approaches will be necessary for more complex geometries, like disk resonator gyroscopes (DRGs) [9, 36].

The remainder of the paper is organized as follows. In section 2 we present a summary of the modeling background required for systematic tailoring of the gyroscope nonlinear dynamic behavior. In section 3 we describe optimization of the gyroscope sensitivity  $S_{\Omega}$ , achieved by the described alterations of the gyroscope layout. The significance of our results and their applicability to modern ring/disk resonating gyroscopes is described in section 4 and concluding remarks are given in section 5.

# 2. Modeling and analytical framework

In this section we outline and extend the theoretical framework developed in [10] to describe nonlinear behavior in ring/disk resonating gyroscopes, with a focus on Duffing and dispersive nonlinearities. The model and approach are generalized to account for non-uniform geometries of the resonator body and electrode gap so that these can be altered by design to systematically improve the gyroscope response. The focus is on demonstrating the applicability of the proposed optimization methods for gyroscopes with rather simple geometries, such as that described in [20], which do not require sophisticated numerical techniques for their analysis, so that one can describe their geometric variations in terms of Fourier series and use the Fourier coefficients for the optimization variables. In section 4, we discuss how one would apply the proposed tuning methods for gyroscopes with more complicated geometries, such as DRGs [9, 36].

# 2.1. General approach

In what follows, we consider a model for a micromechanical gyroscope composed of a thin ring of nominal radius R, nominal radial thickness h, and uniform out-of-plane thickness b,

with  $h, b \ll R$ , which allows one to use shallow shell bending theory for the mechanics of the ring. The outer rim of the ring is surrounded by cyclically placed segmented electrodes with nominal gap  $\Delta$  between the ring and electrodes, with  $\Delta \ll R$ , b, so that a parallel plate analysis can be employed to model the electrostatic force from each electrode. Due to its symmetry, the ring has a pair of in-plane degenerate elliptical eigenmodes, whose dynamics we describe by modal coordinates A and B and mode shapes expressed as  $\Phi_A(r,\theta) = \cos 2\theta$  and  $\Phi_B(r,\theta) = \sin 2\theta$ , where r and  $\theta$  are the radial and azimuthal polar coordinates respectively; see figure 1.

We further designate these gyroscopic modes as the drive, A, and sense, B, modes, respectively, which have nearly equal eigenfrequencies,  $\omega_A \approx \omega_B$  (equal in the ideally symmetric case). The ring vibration and motion are assumed to occur in plane. The ring vibration is excited and detected by means of an electrostatic actuation/sensing scheme that utilizes interactions between the resonator body and the electrodes. We also assume that the ring is spinning with a constant angular rate  $\Omega$  about its axis of symmetry, resulting in Coriolis coupling of the sense and drive modes during vibration and spin. We assume that  $\Omega \ll \omega_A, \omega_B$ , which is readily achieved by design. The amplitudes of vibration are assumed to be small compared to the gyroscope thickness and gap size, that is |A|,  $|B| \ll h$ ,  $\Delta$ . Note that in this formulation both the thickness and electrode gap vary,  $h(\theta)$  and  $\Delta(\theta)$ , and that the stated assumptions must hold throughout the resonator body. It is further assumed that the gyroscope is made of a linear elastic isotropic material with uniform mass density  $\rho^6$ . We use finite deformation kinematics in the following development, details of which are given in [10]. Denoting  $u = u(\theta, t)$  and  $v = v(\theta, t)$ as the radial and circumferential displacements of the ring, and integrating over the body of the gyroscope, the kinetic energy is expressed as

$$T = \frac{\rho b}{2} \iint_{S_{\nu}} [(\dot{u} - \nu \Omega)^2 + (\dot{v} + (r + u)\Omega)^2] r dr d\theta \qquad (1)$$

and the elastic strain energy is given by

$$U_{m} = \frac{b}{2} \iint_{S_{g}} (\sigma_{rr} \epsilon_{rr} + \sigma_{\theta\theta} \epsilon_{\theta\theta} + \sigma_{r\theta} \epsilon_{r\theta}) r dr d\theta, \qquad (2)$$

where  $\varepsilon_{ij}$  and  $\sigma_{ij}$  represent the mechanical strains and stresses occurring in the ring body, respectively, which are related through a linear Hooke's law with modulus of elasticity E, and the integration is carried out over the gyroscope area  $S_g$  perpendicular to  $\bar{\Omega}$ . The electrostatic potential arises from a DC bias voltage  $V_{DC}(\theta)$  and an AC drive voltage  $V_{AC}(\theta,t)$  acting between the electrodes and the outer gyroscope surface and is expressed by expanding in  $u/\Delta$ , up to 4th order to be mathematically consistent with our treatment of elastic strain energy, and integrating over the circumference, yielding

<sup>&</sup>lt;sup>6</sup> Note that many gyroscopes are made from single crystal Si which is anisotropic; this feature can be easily accounted for in a finite element version of the proposed approach.

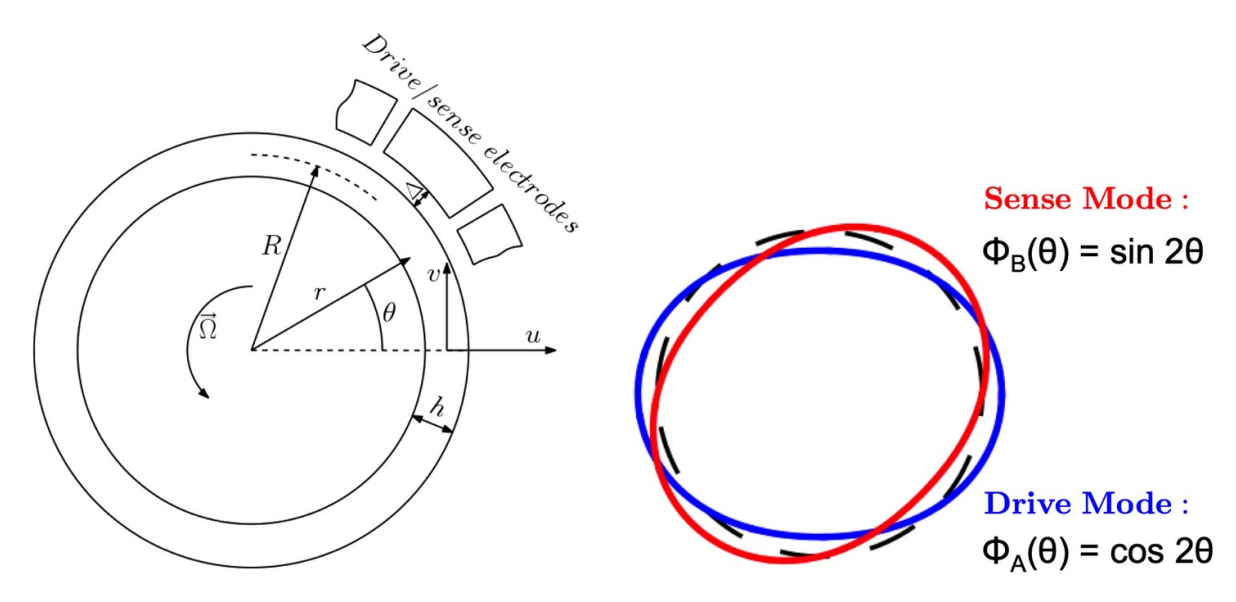


**Figure 1.** Left: schematic representation of the micromechanical ring resonating gyroscope with the electrostatic actuation/sensing scheme using segemented electrodes. Right: degenerate elliptical eigenmodes of the ring resonating gyroscope; dashed line is the nominal static ring configuration, [10].

$$U_e \approx -\frac{\epsilon_0 bR}{2} \sum_{n=0}^{4} \int_0^{2\pi} d\theta (V_{DC} + V_{AC}(\theta, t))^2 \frac{u^n(\theta, t)}{\Delta^{n+1}},$$
 (3)

where  $\epsilon_0 = 8.85 \ F/m$  is the vacuum permittivity. Note that the electrostatic forces cause a circumferential expansion of the ring, but this effect is negligible for realistic devices [10]. The potentials in this model each contribute nonlinearities that have two ultimate effects: an effective Duffing coefficient for each mode and coupling between the modes, of which the dispersive term is of present interest.

In order to investigate the dynamics of the modes of interest, it is assumed that the radial displacement is expressed in terms of the desired modes using modal coordinates *A* and *B* as,

$$u(\theta, t) = A(t)\cos 2\theta + B(t)\sin 2\theta + C(t), \tag{4}$$

where the time-dependent term  $C(t) \approx -(A^2 + B^2)/R$  is included to satisfy periodicity of the gyroscope circumferential displacement, namely,  $v(\theta + 2\pi, t) = v(\theta, t)$ . It is assumed that the ring is inextensible in the circumferential direction, which is valid if the wavelength of the bending vibration modes is large compared to h [37, 38]. This imposes a kinematic constraint that allows one to to express v in terms of u, resulting in a formulation that depends on only the radial displacement field u [10]. The energies are then expressed in terms of the modal expansion, presented by equation (4), and make use of the inextensibility constraint for v, and from the resulting expressions the equations of motion are obtained using a standard Lagrangian approach. In the formulation, it is assumed that the AC drive voltage is aligned with the drive mode  $\cos 2\theta$ , as required for proper operation of the gyroscope. Finally, we must account for dissipation in the system, which is provided by a phenomenological linear damping model added to both modes, of the form  $\frac{\omega_A}{Q_A}\dot{A}$  and  $\frac{\omega_B}{Q_B}\dot{B}$ , or, equivalently,  $2\Gamma_A\dot{A}$  and  $2\Gamma_B\dot{B}$ , where the Q's are the modal quality factors and the  $\Gamma$ 's are the modal decay rates. For proper function of the gyroscope, the Q's are large, or, equivalently, the decay rates  $\Gamma$  are small compared to the vibration frequency, that is,  $\Gamma_i \ll \omega_i$ .

The result of this process is a pair of complicated coupled nonlinear differential equations in *A* and *B* (see the appendix) that have a large number of terms, many of which can be ignored by employing the above-stated assumptions. The outcome of these approximations is that one can essentially decouple the system and solve for the drive mode dynamics while ignoring the influence of the sense mode, primarily because its amplitude is significantly larger than that of the sense mode equation using perturbation techniques, the drive response is used as input for the sense mode dynamics, which is assumed to be in its linear range, that is, its Duffing effect is negligible. However, coupling from the relatively large amplitude drive mode results in both direct and parametric resonant driving of the sense mode. A summary of this process follows.

# 2.2. Drive mode dynamics

Following the general formulation and assumptions presented in the previous section, the simplified equation governing the drive mode, normalized by its effective mass, can be expressed as

$$\ddot{A}\left(1+\mu\frac{A^{2}}{R^{2}}\right)+\frac{\omega_{A}}{Q_{A}}\dot{A}+A\omega_{A}^{2}+A\left(\mu\frac{\dot{A}^{2}}{R^{2}}+(\gamma_{m}+\gamma_{e})\frac{A^{2}}{R^{2}}\right)$$

$$=F\cos(\omega t+\phi_{F}),$$
(5)

where coefficient  $\mu$  results from inertial nonlinearities and coefficients  $\gamma_m$  (>0) and  $\gamma_e$  (<0) are hardening and softening Duffing effects from the mechanical deformation and electrostatic potentials, respectively. Most terms in this equation are affected by the DC voltage. The AC voltage at frequency  $\omega$  results in an effective drive amplitude F and phase  $\phi_F$ . It is important to note that this model ignores backaction of the sense mode on the drive mode, including both the linear coupling that is proportional to  $\Omega B$  that arises from Coriolis effects, as well as those that arise from nonlinear coupling, such as dispersive coupling. This assumption must be carefully considered in systems with degenerate frequencies, and is systematically justified for the present case in [10]. For the near-resonance response, this equation is amenable to standard perturbation techniques. The method of averaging can be used to obtain an approximate steady-state solution of the form  $A(t) = aR\cos(\omega t + \phi + \phi_F)$ , where the following implicit relationship is determined between the normalized amplitude a = |A|/R of the drive mode and both the system and drive parameters,

$$a^2 R^2 \left\{ \frac{\omega_A^4}{Q_A^2} + \left( 2\sigma \omega_A - \frac{3}{4} \gamma a^2 \right)^2 \right\} = F^2, \tag{6}$$

where  $\sigma=\omega-\omega_A$  is the deviation of the excitation frequency from the drive mode eigenfrequency and  $\gamma=\gamma_m+\gamma_e-\frac{2}{3}\mu\omega_A^2$  is the net Duffing coefficient of the drive mode, stemming from elastic, electrostatic, and inertial sources, respectively. For a simple thin ring,  $\mu=\frac{33}{5}$ ,  $\gamma_m=2$   $\omega_A^2$ , and  $\gamma_e$  is negative and tunable with the DC voltage. Equation (6) is a cubic equation in  $a^2$ , which can be solved numerically to obtain frequency response backbone curve of the drive mode under external excitation. It is well-known that there exists a critical drive level corresponding to the onset of nonlinear behavior in the form of bistability, given by  $F_{cr}=\frac{4\omega_A^3}{3Q_A}\sqrt{\frac{2}{Q_A|\gamma|\sqrt{3}}}$ , for which the system response is single-valued when  $F < F_{cr}$  and multivalued for  $F > F_{cr}$ , [39, 40]. An AC drive voltage corresponding to  $F = F_{cr}$  results in a peak amplitude of  $a_{cr} = \frac{2\sqrt{2}\omega_A}{\sqrt{3}Q_A|\gamma|\sqrt{3}}$ , and we use this amplitude as the desired operating level for subsequent analysis. It is clear that reducing the Duffing nonlinearity  $\gamma$  allows for larger operation without bistability.

# 2.3. Sense mode dynamics

The sense mode is assumed to respond with a relatively small amplitude such that it remains in its linear range. This assumption is well-justified in the light of the present study. For example, if the representative ring gyroscope from [20] is exposed to the angular rate  $\Omega \sim 1$  Hz (typical value for the rate grade gyroscopes [1]), and its drive mode is operated at the onset of nonlinearity, the gyroscope sense mode vibration amplitude satisfies  $b \sim 0.1a_{cr}$ , which indicates that the gyroscope sense mode remains in its linear regime. It is excited by the drive mode response A(t) through both Coriolis (linear) terms and dispersive modal coupling. As such, the model

for the response of the sense mode, under the assumptions provided above, is

$$\ddot{B} + \dot{B} \left( \frac{\omega_B}{Q_B} + C_\Gamma \frac{A\dot{A}}{R^2} \right) + B\omega_B^2 + B \left( C_d \frac{A^2}{R^2} + C_1 \frac{\dot{A}^2}{R^2} + C_2 \frac{A\ddot{A}}{R^2} \right)$$

$$= C_\Omega \Omega \dot{A}, \tag{7}$$

which is a linear equation in B(t) with both direct and parametric excitation from A(t). In the above equation, coefficients  $C_i$  are numerical constants that depend on the resonator geometry; for a simple ring, the reader can find their values in the appendix. Note that the direct excitation is from Coriolis effects (the usual input to the sense mode) and is at frequency  $\omega$  while the parametric driving is expressed in several terms that arise from nonlinear modal coupling, all of which result in parametric excitation at frequency  $2 \omega$  from the drive mode, as required for parametric amplification. The method of averaging can again be employed to obtain an expression for the normalized sense mode amplitude b = |B|/R in terms of the system parameters and the drive mode amplitude a, as follows

$$|b| = |C_{\Omega}| \Omega a Q_B \frac{\omega}{2} \frac{\sqrt{\omega^2 \omega_B^2 + Q_B^2 (\omega_n^2 - \omega^2 + \lambda)^2}}{|\omega^2 \omega_B^2 + Q_B^2 (\omega_n^2 - \omega^2)^2 - \lambda^2 Q_B^2|}, \quad (8)$$

where  $\omega_n = \sqrt{\omega_B^2 + \frac{1}{2}a^2(C_d + \omega^2(C_1 - C_2))}$  is the natural frequency of the sense mode shifted from its nominal value  $\omega_B$  due to the coupling to the drive mode and  $\lambda = \frac{1}{4}a^2(C_d + \omega^2(C_\Gamma - C_1 - C_2))$  is the strength of parametric pumping from the drive mode. For a representative ring resonating gyroscope, such as that described in [20],  $|C_d|/\omega_B^2 \equiv |\kappa|/\omega_B^2 \gg |C_1|, |C_2|, |C_\Gamma|$ , which allows us to neglect these small terms when considering dynamics of the sense mode. Importantly, the vibration amplitude of the sense mode can be expressed in terms of the gain provided by the parametric pumping from the drive mode which amplifies the sense mode signal compared to it value from Coriolis effects alone. While detailed examples are worked out in [10], demonstrating and quantifying the desired effect, here the focus is on enhancing and optimizing this effect.

# 2.4. Objective function

In this section we generalize the approach presented in [10] to allow for non-uniformities in the design of the ring and the electrodes. Specifically, we allow parameters h and  $\Delta$  to depend on  $\theta$  and then use the mode shapes of the uniform device to project the energies onto modal amplitudes A and B. As stated in section 1, we are interested in manipulating two specific coefficients in the gyroscope equations of motion: the dispersive inter-modal coupling strength  $\kappa$  with the goal of maximizing it, and the drive mode Duffing nonlinearity  $\gamma$ , with the objective to minimize it. These coefficients define general anharmonic terms in the overall gyroscope potential energy,

which when written in terms of the modal coordinates A and B, can be expresses as,

$$U(A,B) = \frac{1}{2}k(A^2 + B^2) + \frac{1}{4}\gamma'(A^4 + B^4) + \frac{1}{2}\kappa'A^2B^2, \quad (9)$$

where all coefficients depend on both elastic and electrostatic effects. It is important to reiterate that the proposed alterations have the important feature of not breaking the symmetry of the gyroscopic drive and sense modes, so that the stiffness parameters, including the Duffing coefficients, are the same for both modes, i.e.  $k_A = k_B = k$  (linear stiffness coefficient) and  $\gamma_A' = \gamma_B' = \gamma'$  (Duffing term). While the modal mass affects the coefficients of interest in the full model, we focus our analysis on the normalized  $\kappa$  and  $\gamma$  coefficients in the gyroscope potential energy, given in sections 3.1 and 3.2, since it is found that the contributions from inertial nonlinearities are quite insensitive to the considered alterations in the gyroscope geometry and are clearly independent of the gyroscope electrostatic setup [10]. Finally, in section 3.3 we consider the effective modal mass in the optimization process, defined as the coefficient of the term  $\propto A^2$  in the gyroscope kinetic energy, which, as expected, also depends on the gyroscope geometry.

Due to the dispersive nature of the coupling between the gyroscopic drive and sense modes, the gyroscope sense mode response depends on both  $\kappa$  and  $\gamma$ , and this dependence generally has a complicated form even in the approximation of linear sense mode response, see equation (8), where the dependence on  $\gamma$  is implicit through the vibration amplitude of the drive mode a. Given our goals of simultaneously maximizing the gyroscope angular rate sensitivity and the gyroscope dynamic range, which are competing nonlinear effects, we define the objective function for our optimization problem to be the gyroscope output sensitivity to the external angular rate

$$S_{\Omega} = \frac{|b|}{\Omega} \bigg|_{a = a_{cr}} \tag{10}$$

when the gyroscope drive mode is operated at the  $a_{cr} \propto |\gamma|^{-1/2}$  condition on its frequency response, that is, at the onset of nonlinearity [39, 41]. While this may not be the preferred operating condition for some gyroscopes, it provides a meaningful and physically intuitive constraint for the present optimization problem. For real-world applications, a reasonable alternative may be to operate at some level less than, and proportional to,  $a_{cr}$ .

For gyroscopes where the dominant nonlinear effects are electrostatic, i.e.  $\gamma$ <0, such as the case in [20], we proceed by using equation (8) along with the drive mode operating conditions:

$$a = a_{cr} = \frac{2\sqrt{2}\omega_A}{\sqrt{3Q_A|\gamma|\sqrt{3}}},$$

$$\omega = \omega_{cr} = \omega_B \left(1 - \frac{\sqrt{3}}{2Q_B}\right), Q_B \gg 1,$$
(11)

and arrive at the following expression for the objective function

$$S_{\Omega} = \frac{16}{5\sqrt{6\sqrt{3}}} \sqrt{\frac{Q_B}{|\gamma|}} \frac{\sqrt{1 + \left(\sqrt{3} - \frac{2K}{\sqrt{3}}\right)^2}}{\left|1 + \left(\sqrt{3} - \frac{4K}{3\sqrt{3}}\right)^2 - \frac{4}{27}K^2\right|}, \quad (12)$$

where  $Q_B$  is the sense mode quality factor (assumed to be equal to the drive mode quality factor  $Q_A$  due to modal symmetry),  $K = |\kappa'/\gamma'| = |\kappa/\gamma|$  is the ratio of nonlinear stiffness terms, and  $\gamma = \gamma' R^2/k$ ,  $\kappa = \kappa' R^2/k$  are nondimensional nonlinear stiffness coefficients. Figure 2 illustrates an example of the gyroscope angular rate sensitivity  $S_{\Omega}$  as a function of nonlinear stiffness coefficients  $\gamma$  and  $\kappa$ .

Analysis of equation (12) reveals that  $S_{\Omega} \to \infty$  for  $K^* = 3$ , denoted by the red line in figure 2. Physically, this corresponds to the case where sense mode response becomes unstable due to parametric excitation coming through dispersive coupling to the drive mode. However, this is an artifact of the model used in section 2.3, where the sense mode dynamics was represented by that of a linear system. In particular, the expression for  $S_{\Omega}$  shown in equation (12) has been obtained following the assumption that the external angular rate  $\Omega \ll \omega_B$  and, as a result, the gyroscope sense mode operates in its linear regime. In practice, however, when  $K \to K^*$ , the sense mode amplitude grows beyond its value at the onset of nonlinearity,  $b_{cr} = a_{cr}$ , and equation (8) is no longer a valid representation of the sense mode dynamics. In the light of our goal (maximizing the gyroscope rate sensitivity), we assume that the gyroscope is exposed to an external angular rate that results in the gyroscope sense mode vibration amplitude to be below its critical value. It is also important to highlight that equation (12) and, thus,  $K^* = 3$  were obtained under the assumption  $Q_B \gg 1$ . While this is a very reasonable assumption for high-Q resonant systems, it is critical that any finite  $Q_B$  will still result in  $S_{\Omega} \to \infty$  for some finite value of K; for example,  $Q_B = 1200$ [20] results in  $K^* = 2.96, 3.04$ , thus allowing us to apply the subsequent analysis with this high-Q approximation in mind.

In summary, from figure 2 it follows that our goal is to alter the ring geometry and/or electrostatic setup in such a way that resonator nonlinear parameters move from the 'black diamond' towards the red line, that is, to higher angular rate sensitivity. Of course, how the design moves in this space depends on the physical model and what alterations are being made. This is considered next.

# 3. Mechanical and electrostatic optimization methods for tailoring gyroscope nonlinearities

In this section we analyze three different approaches for manipulating the magnitude of nonlinear dispersive coupling  $|\kappa|$  and the modal Duffing nonlinearity  $|\gamma|$  with the objective to maximize the sensitivity  $S_{\Omega}$  of a micromechanical gyroscope with respect to the external angular rate. Specifically, in the following subsections we consider tailoring of the aforementioned gyroscope nonlinearities via a non-uniform distribution

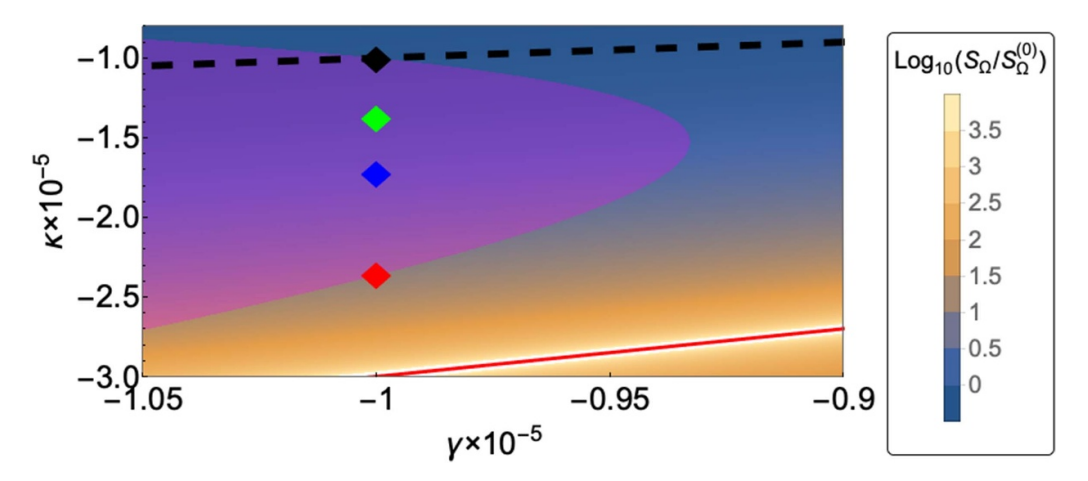


Figure 2. Gyroscope angular rate sensitivity normalized with respect to its nominal value obtained for the uniform ring with  $\kappa = \gamma \approx -10^5$  (black diamond); quality factors of the gyroscope drive and sense modes are assumed  $Q_A = Q_B = 1200$  [20]. The red line corresponds to the case when  $S_\Omega \to \infty$ , that is, the parametric instability according to the linear approximation for the gyroscope sense mode adopted in section 2.3. The black dashed line is the locus of points where  $\kappa = \gamma$ , that is, K = 1. The magenta region is the  $\kappa = \gamma$  range that is accessible via modifications in the gyroscope biasing scheme and electrode shape, as detailed in sections 3.1 and 3.2. The blue and green diamonds represent cases of maximizing  $|\kappa|$  while maintaining gyroscope dynamic range  $(\gamma)$  via alternations in the gyroscope biasing scheme (section 3.1) and electrode uniformity (section 3.2), respectively. The combination of these two adjustments in the gyroscope configuration results in nearly 12-fold increase in the gyroscope angular rate sensitivity without sacrificing its dynamic range, as depicted by the red diamond.

of the bias voltage  $V_{DC}$  among the gyroscope electrodes, by an angle-dependent electrode gap width  $\Delta(\theta)$ , and by an angle-dependent thickness of the gyroscope ring  $h(\theta)$ , respectively. Note that in all these methods we only consider modifications that have at least 8-fold rotational symmetry relative to the z-axis of the gyroscope. As we mentioned above, this essential constraint ensures the inherent symmetry of the gyroscopic vibrational modes, which allows one to avoid additional problems associated with matching the modal natural frequencies. It also maintains symmetry in the Duffing nonlinearities.

# 3.1. Nonlinear electrostatic tuning by a non-uniform bias voltage

We start with a relatively simple method of electrostatic tuning, which is frequently used for modifying the vibration frequency and/or motional impedance of electrostatic MEMS resonators by controlling the bias voltage. In the present case, however, we are interested in modifying the gyroscope *nonlinear* parameters  $\kappa$  and  $\gamma$ . Without any alterations of the gyroscope electrostatic actuation/sensing geometrical setup,  $\kappa$  and  $\gamma$  for a thin ring gyro are found to be, see appendix,

$$\kappa = \gamma = \frac{6R^2}{5\rho} \left( \frac{Eh^2}{R^6} - \frac{\epsilon_0 V_{DC}^2}{h\Delta^5} \right),\tag{13}$$

where E is the Young's modulus of the gyroscope material and the rest of parameters are defined in section 2. From equation (13) it follows that a uniform increase/decrease of the bias voltage changes both coefficients simultaneously. From figure 2, however, it follows that the  $\kappa = \gamma$  condition can provide only minor increase of the gyroscope sensitivity by a uniform decrease of  $V_{DC}$  since  $S_{\Omega}$  scales as  $|\gamma|^{-1/2}$  in this case, see equation (12). Furthermore, lowering the bias

voltage results in a decrease of the gyroscope sense current that, in turn, reduces the gyroscope signal-to-noise ratio. In contrast, our goal is to maximize  $S_{\Omega}$ , which is accomplished by increasing  $|\kappa|$  while minimizing  $|\gamma|$ , thereby moving toward the lower right corner in figure 2. As such, we attempt to achieve  $|\kappa| \geq |\gamma|$ , i.e. below the black dashed line on figure 2, when considering the case of a non-uniform bias voltage, i.e.  $V_{DC} = V_{DC}(\theta)$ .

Frequently, MEMS ring/disk resonating gyroscopes are designed to have 8 N electrodes ( $N \ge 1$ ) along the circumference in order to be able to support and monitor  $\sin 2\theta$  and  $\cos 2\theta$  in-plane elliptical vibrational modes. In this case, the nonlinear electrostatic tuning method, assuming that modal frequencies are already matched, results in different values of bias voltage applied to different electrodes, i.e.  $V_{DC} = V_{DC}(k)$ , where k is the electrode number. Keeping in mind the symmetry of the gyroscopic modes, it becomes clear that the 8electrode configuration can support only uniform distribution of the bias voltage  $V_{DC}$ , which, as we discussed above, is of limited interest. Therefore, in order to show the effect of  $V_{DC}(k)$  on resonator nonlinearities, we assume that the gyroscope design has 8 N segmented electrodes ( $N \ge 2$ ), in which case the electrostatic potential energy, defined in equation (3) can be rewritten as

$$U_e \approx -\frac{\epsilon_0 bR}{2} \sum_{k=1}^{8N} \sum_{n=0}^{4} \int_{\theta_k - \psi}^{\theta_k + \psi} d\theta V^2(k, t) \frac{u^n(\theta)}{\Delta^{n+1}}, \tag{14}$$

where  $\theta_k$  is the angular position of the kth electrode center,  $2\psi$  is the circumferential length of each electrode (in radians), and  $V(k,t) = V_{DC}(k) + V_{AC}(k,t)$  where both  $V_{DC}$  and  $V_{AC}$  are now functions of the electrode number.

Clearly, a non-uniform DC bias voltage distribution only affects  $\kappa$  and  $\gamma$  through their electrostatic contributions,  $\kappa_e$  and

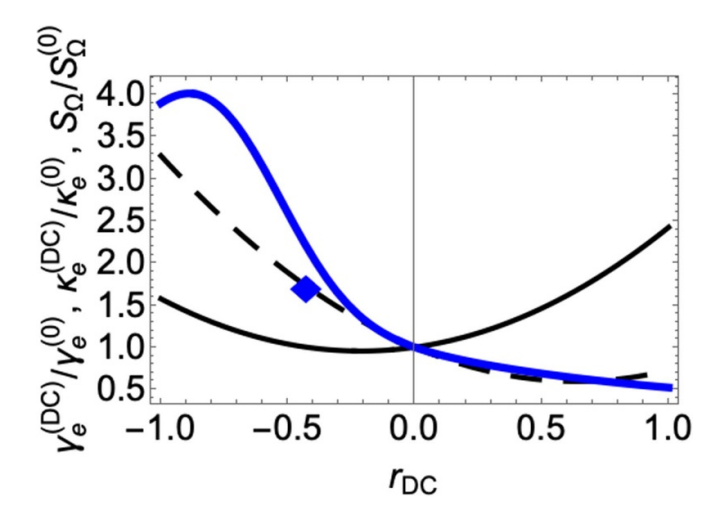


Figure 3. Dependence of the electrostatic components of the dispersive coupling strength  $\kappa_e$  (dashed curve), the Duffing nonlinearity  $\gamma_e$  (solid black curve), and the normalized objective function  $S_{\Omega}^{(DC)}/S_{\Omega}^{(0)}$  (solid blue curve) as functions of the non-uniformity in the bias voltage as represented by  $r_{DC}$ . The blue diamond represents the case of maximizing  $|\kappa|$  while maintaining gyroscope dynamic range, i.e.  $\gamma_e^{(DC)} \leq \gamma_e^{(0)}$ , and corresponds to the similar point indicated in figure 2.

 $\gamma_e$ , determined by the coefficients of the terms  $\propto A^2B^2$  and  $\propto A^4$  in equation (14). In order to illustrate the nonlinear electrostatic tuning method using these electrodes, we consider the specific case when N=2, as in [14], and assume the following distribution of the bias voltage

$$V_{DC}(k) = V_{DC}(1 + (-1)^k r_{DC}), \quad k = 1, ..., 16.$$
 (15)

Restricting ourselves to the case of the commonly used uniform electrode gap size, we obtain

$$\frac{\kappa_e^{(DC)}}{\kappa_e^{(0)}} \approx 1 - \frac{4}{\pi} r_{DC} + r_{DC}^2, \tag{16a}$$

$$\frac{\gamma_e^{(DC)}}{\gamma_e^{(0)}} \approx 1 + \frac{4}{3\pi} r_{DC} + r_{DC}^2,$$
 (16b)

where  $\kappa_e^{(0)} = \gamma_e^{(0)}$  are the nominal values of the coupling strength and Duffing nonlinearity when  $r_{DC} = 0$ . Note that the magenta region of figure 2 is determined by bounding non-uniformity parameters, including  $-1 < r_{DC} < 1$  (plus a bound on another parameter introduced in the next section). The dependence of  $\kappa_e$  and  $\gamma_e$  on the variation in the gyroscope bias voltage  $r_{DC}$  are represented in equations (16a) and (16b) and the corresponding behavior of these quantities and the resulting sensitivity  $S_\Omega$  as a function of  $r_{DC}$  are shown in figure 3.

In ring resonating gyroscopes, the electrostatic forces from the actuation/sensing scheme frequently dominate the nonlinear dynamic behavior of the gyroscopic vibrational modes, so that  $\kappa \approx \kappa_e$  and  $\gamma \approx \gamma_e$ . In this case, figure 3 clearly shows that when  $r_{DC} < 0$ , one can achieve up nearly 4-fold increase

in  $S_{\Omega}$ . Also note that  $|\gamma|$  decreases for  $r_{DC} \in (-4/3\pi, 0)$ , but increases, although slower than  $|\kappa|$ , for  $r_{DC} \in (-1, -4/3\pi)$ . Assuming, for instance, that we choose  $r_{DC} = -4/3\pi$ , which maintains  $\gamma_e$  and, thus, the gyroscope dynamic range, we achieve an approximately 72\% increase of the modal coupling strength and, as a result, more than 2-fold increase of the gyroscope sensitivity. Note that the electrostatic tuning method described here also shifts the natural frequencies of the gyroscopic vibrational modes. However, since the gyroscope linear stiffness is dominated by the mechanical elastic effects, this correction to the modal frequencies is rather small. In fact, the electrostatic correction to the modal linear stiffness is  $\propto r_{DC}^2$ and, importantly, is the same for both modes. A recent finite element study by the authors for a particular ring geometry has confirmed the quantitative accuracy of these curves, lending credence to the approach [35]. We next consider the effects of geometric alterations to the gyro body and the electrode gap.

# 3.2. Effects of a non-uniform electrode gap size

In this section we assume that  $V_{DC}=const$  across all the gyroscope electrodes and consider the effects of a non-uniform electrode gap size on the magnitudes of  $\kappa$ ,  $\gamma$ , and  $S_{\Omega}$ . In contrast to bias-based tuning using segmented electrodes, the electrode gap size can be varied in a continuous fashion along the gyroscope circumference, i.e.  $\Delta=\Delta(\theta)$ , as depicted in figure 4(b). In this case the gyroscope electrostatic potential energy becomes

$$U_{el} \approx -\frac{\epsilon_0 bR}{2} V_{DC}^2 \sum_{n=0}^4 \int_0^{2\pi} d\theta \frac{u^n(\theta)}{\Delta^{n+1}(\theta)}.$$
 (17)

As mentioned above, the variation in the electrode gap size should also possess at least 8-fold rotation symmetry in  $\theta$  in order to ensure that the gyroscopic modes remain degenerate, so that we express the gap as

$$\Delta(\theta) = \sum_{k=0}^{\infty} \Delta_k \cos(8k\theta), \tag{18}$$

where  $\Delta_k$  are Fourier coefficients that become design space variables. In this work, in order to demonstrate the applicability of the method we consider the simplest case that yields a non-trivial result:

$$\Delta(\theta) = \Delta_0(1 + r_\Delta \cos(8\theta)). \tag{19}$$

Of course, this harmonic will offer the dominant effect possible by the use of a single harmonic. From a physical standpoint, the variation  $r_{\Delta}$  must satisfy  $|r_{\Delta}| < 1$ . In practice, however, the constraint on  $|r_{\Delta}|$  becomes even stronger due to constraints imposed by the chosen microfabrication process, in order to ensure successful release of the resonator and avoid resonator failure due to stiction and/or electrostatic pull-in. In the present study we restrict  $-0.2 < r_{\Delta} < 0.2$ , which is used, along with bounds on  $r_{DC}$ , to determine the magenta (feasible) region shown in figure 2. Assuming that the gaps between individual electrodes are small, we expand the denominator in

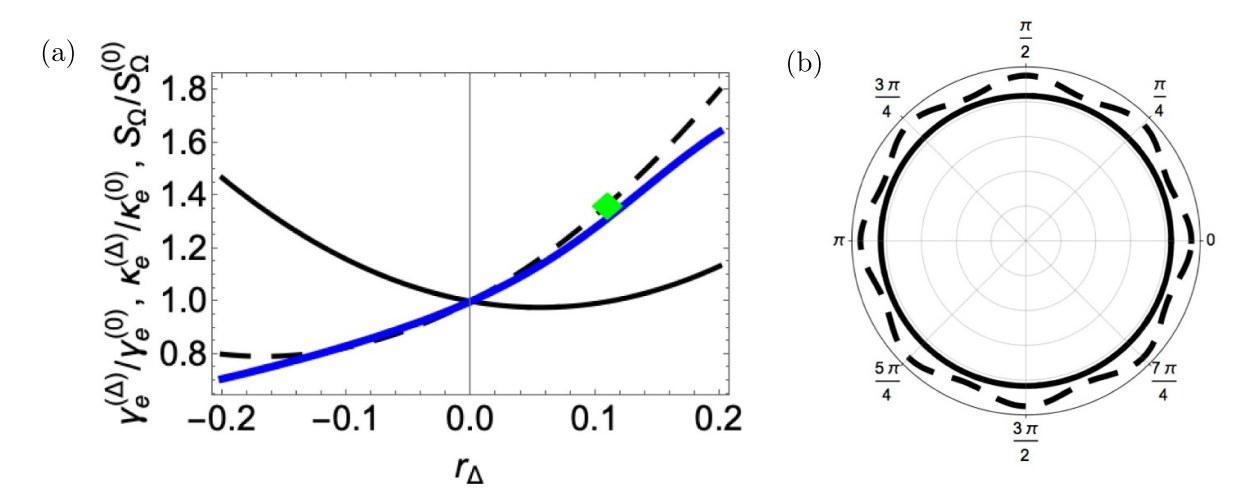


Figure 4. Manipulating gyroscope nonlinearities via a non-uniform electrode gap size. (a) Dependence of the electrostatic components of the dispersive coupling strength  $\kappa^e$  (dashed curve), the Duffing nonlinearity  $\gamma^e$  (solid black curve), and the normalized objective function  $S_{\Omega}^{(\Delta)}/S_{\Omega}^{(0)}$  (solid blue curve) as functions of the variation in the electrode gap size  $r^{\Delta}$ . The green diamond represents the case of maximizing  $|\kappa|$  while maintaining gyroscope dynamic range, i.e.  $\gamma_e^{(\Delta)} \leq \gamma_e^{(0)}$ , and corresponds to the similar point indicated in figure 2. (b) Schematic representation of a ring resonating gyroscope with a nonuniform electrode gap size with  $r_{\Delta} = 0.4$ . The solid circle represents the outer boundary of the gyroscope body; the dashed curve represents the inner boundary of the attendant electrodes.

equation (17) in Taylor series up to the second order in  $r_{\Delta}$  and obtain corrections to the coefficients of the electrostatic dispersive coupling and Duffing nonlinearity in the form

$$\frac{\kappa_e^{(\Delta)}}{\kappa_e^{(0)}} \approx 1 + \frac{5}{2}r_\Delta + \frac{15}{2}r_\Delta^2,\tag{20a}$$

$$\frac{\gamma_e^{(\Delta)}}{\gamma_e^{(0)}} \approx 1 - \frac{5}{6} r_{\Delta} + \frac{15}{2} r_{\Delta}^2. \tag{20b}$$

The dependence of  $\kappa_e$  and  $\gamma_e$  on the variation in the electrode gap size  $r_{\Delta}$  and the corresponding behavior of  $S_{\Omega}$  are shown in figure 4(a). From this figure it immediately follows that the case with  $r_{\Delta}>0$  becomes of significant importance for gyroscopes whose dynamic behavior in the nonlinear regime is dominated by electrostatic effects. Indeed, when  $r_{\Delta}>0$ , the dispersive coupling strength  $|\kappa_e|$  grows faster than the Duffing nonlinearity  $|\gamma_e|$ . Furthermore,  $\gamma_e^{(\Delta)}/\gamma_e^{(0)} < 1$  for  $r_{\Delta} \in (0,1/9)$ . Assuming, as before, that one desires to maintain the dynamic range of the uniform case, we choose  $r_{\Delta}$  = 1/9 and achieve an increase in  $|\kappa_e|$  of  $\approx 37\%$  by a simple alteration of the shape of the gyroscope electrodes at the design stage, as depicted in figure 4(b). As follows from figure 2, this increase of the coupling strength should lead to an approximately 32% increase of the sensitivity when the gyroscope drive mode is operated at the onset of the Duffing nonlinearity. It is worth noting, however, that uncertainties in microfabrication process are expected to limit benefits provided by alteration of the electrostatic gap due to the fact that there is a natural variation of electrostatic gap along the resonator body. Avoiding this limitation might be a non-trivial challenge forcing designers to increase  $r_{\Delta}$  beyond 1/9 at the expense of reducing the gyroscope dynamic range and, thus, revisiting tradeoffs in device performance.

### 3.3. Shape optimization of the gyroscope body

Lastly, we show how one can alter the mechanical contributions to  $\kappa$  and  $\gamma$  in micromechanical ring/disk resonating gyroscopes by modifying the shape of the gyroscope body. Here we illustrate this technique by manipulating the nonlinear stiffness parameters of a thin spinning ring, discussed in section 2, by modifying the ring radial thickness along the gyroscope circumference. Similar to the electrode gap size variation described in section 3.2, we require that the ring radial thickness be periodic in  $\theta$ , with the period being at most  $\pi/4$  in order to preserve the symmetry of the drive and sense modes. Mathematically we express  $h(\theta)$  as

$$h(\theta) = \sum_{k=0}^{\infty} h_k \cos(8k\theta), \tag{21}$$

where  $h_k$  are Fourier coefficients chosen to meet the desired optimization goal. Of course, the ring thickness must satisfy fabrication and other restrictions, which will be satisfied here by assuming  $h_k \ll h_0$  for k > 1. Incorporation of  $h(\theta)$  in the dynamic model for the ring resonating gyroscope modifies the expressions obtained earlier for the gyroscope kinetic and mechanical potential energies, as follows

$$T = \frac{\rho bR}{2} \int_{0}^{2\pi} d\theta [(\dot{u} - v\Omega)^{2} + (\dot{v} + (r+u)\Omega)^{2}] h(\theta), \quad (22a)$$

$$U_m = \frac{Eb}{24R^3} \int_0^{2\pi} d\theta \left[ u + \frac{\partial^2 u}{\partial \theta^2} - \frac{1}{2R} \left( \frac{\partial u}{\partial \theta} \right)^2 \right]^2 h(\theta)^3. \quad (22b)$$

As noted in section 2, modifications in the resonator geometry affect  $\kappa$  and  $\gamma$  in two ways. First, as follows from equation (22a), the non-uniformity of the ring radial thickness affects the effective modal mass, that is, the coefficient of the term  $\propto \dot{A}^2$  in the gyroscope kinetic energy projected

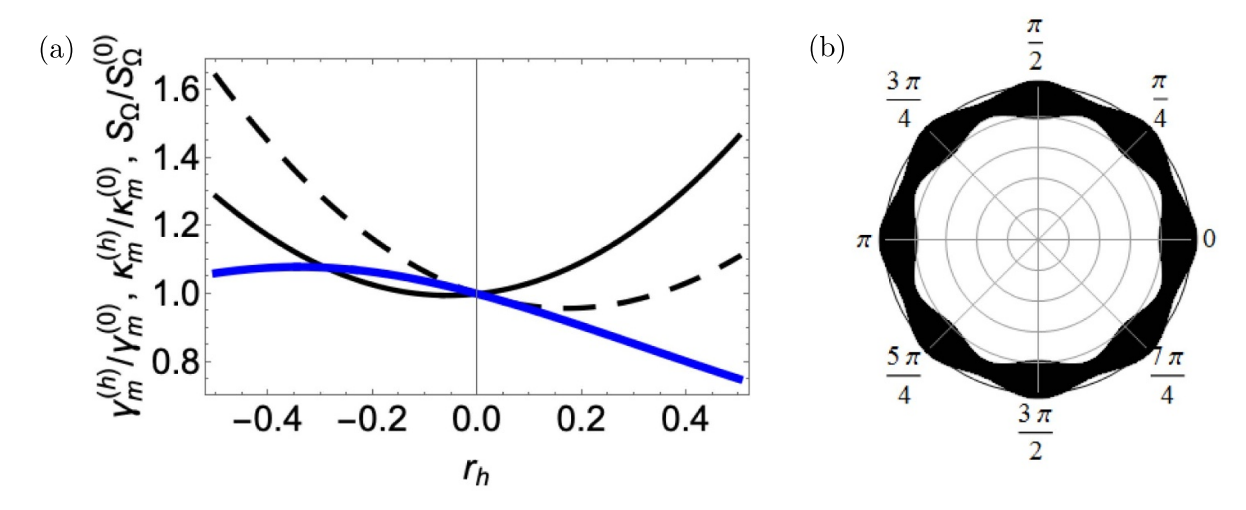


Figure 5. Manipulating nonlinear parameters of a thin spinning ring by varying the radial ring thickness  $h(\theta)$ . (a) Dependence of the mechanical components of the dispersive coupling strength  $\kappa_m$  (dashed curve), the Duffing nonlinearity  $\gamma^{\rm m}$  (solid black curve), and the normalized objective function  $S_{\Omega}^{(h)}/S_{\Omega}^{(0)}$  (solid blue curve, under the assumption that mechanical nonlinearities are dominant) on the ring thickness non-uniformity parameter  $r^{\rm h}$ . (b) Representative geometry of the ring resonating gyroscope with the nonuniform radial thickness with  $r_h < 0$ . Electrodes, which have uniform gap and are therefore similarly wavy, are omitted for clarity.

onto vibrational modes. Additionally,  $h(\theta)$  changes the stiffness coefficients of the terms  $\propto A^2B^2$  (dispersive coupling) and  $\propto A^4$  (Duffing) in the gyroscope potential energy due to elastic deformations of the ring. By accounting for these two effects, we can express these contributions to the mechanical components of  $\kappa$  and  $\gamma$  as

$$\kappa_{m} = \frac{2E}{\rho R^{6}} \frac{\int_{0}^{2\pi} d\theta (1 + \sin^{2} 4\theta) h^{3}(\theta)}{\int_{0}^{2\pi} d\theta (1 + 3\cos^{2} 2\theta) h(\theta)},$$
 (23a)

$$\gamma_{m} = \frac{2E}{3\rho R^{6}} \frac{\int_{0}^{2\pi} d\theta (1 + 4\sin^{2}2\theta + 4\sin^{4}2\theta) h^{3}(\theta)}{\int_{0}^{2\pi} d\theta (1 + 3\cos^{2}2\theta) h(\theta)}, \quad (23b)$$

from where it immediately follows that if the ring radial thickness is constant, i.e.  $h(\theta) = h_0$ , then  $\kappa_m = \gamma_m$ , as expected.

To demonstrate the effect of a non-uniform ring radial thickness, we consider the simple single harmonic case for which  $h_k = 0$  for  $k \ge 2$  in equation (21). In this case we define  $r_h = h_1/h_0 < 1$  and expand equations (23a) and (23b) in a Taylor series in  $r_h$ , yielding

$$\frac{\kappa_m^{(h)}}{\kappa_m^{(0)}} \approx 1 - \frac{1}{2}r_h + \frac{3}{2}r_h^2 - \frac{1}{8}r_h^3,$$
(24a)

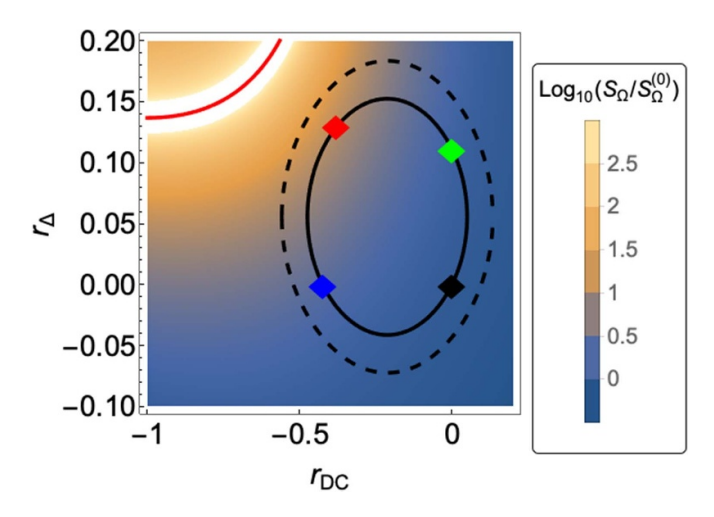
$$\frac{\gamma_m^{(h)}}{\gamma_m^{(0)}} \approx 1 + \frac{1}{6}r_h + \frac{3}{2}r_h^2 + \frac{1}{24}r_h^3.$$
 (24b)

Figure 5(a) illustrates the dependence of  $\kappa_m$ ,  $\gamma_m$ , and  $S_{\Omega}^{(h)}/S_{\Omega}^{(0)}$  on  $r_h$  under the assumption that mechanical nonlinearities are dominant, which could be the case for resonators

that employ alternative transduction methods, e.g. piezoelectricity. From figure 5(a), it also follows that improvement in the gyroscope angular rate sensitivity can be achieved if we modify the ring radial thickness with  $r_h < 0$ ; see figure 5(b). Physically, this case corresponds to thinning the segments of the ring that experience the largest deflections in the radial direction as it vibrates in the drive and sense modes and adding material between those segments. Specifically, following the same line of thought as in sections 3.2 and 3.1, choosing  $r_h = -2/(9+4\sqrt{2})$  preserves the value of  $\gamma_m$ , thus, maintaining the gyroscope dynamic range and increases  $\kappa_m$  by approximately 7% leading to the overall improvement in the gyroscope sensitivity by only 4%. While these results are clearly less impressive than those obtained from electrostatic tuning methods, this mechanical optimization approach should not be overlooked when optimizing gyroscopes with relatively simple geometries of the resonator body, since they are simple to implement [20]. Also, such mechanical effects may dominate for other geometries, such as disks.

# 3.4. Combining the approaches

The three optimization methods discussed above can be used simultaneously in order to further optimize the performance of the ring/disk resonating gyroscope. Assuming, for example, that the nonlinear behavior of the gyroscope is primarily determined by electrostatic forces (which is frequently the case), i.e.  $|\kappa_e|\gg |\kappa_m|$  and  $|\gamma_e|\gg |\gamma_m|$ , one can apply both modification of the electrode gap size and the bias voltage along the gyroscope circumference. Figure 6 depicts a situation where both effects are taken into account. Specifically, following the results of sections 3.1 and 3.2, one should be able to preserve the gyroscope dynamic range while achieving nearly 12-fold increase of the gyroscope sensitivity. On the other hand, by sacrificing the gyroscope dynamic range just a



**Figure 6.** Improvement in the angular rate sensitivity  $S_{\Omega}$  of a free spinning ring as a function of the bias voltage and electrode gap modifiers. The red curve represents the critical case  $(S_{\Omega} \to \infty)$ . The black solid and dashed curves are the loci of the points where  $\gamma = \gamma^{(0)}$  and  $\gamma_e = 1.05 \gamma_e^{(0)}$ , respectively. Black, blue, green, and red diamonds represent, respectively, the following modifications in the gyroscope electrostatic setup: no modifications (uniform case), bias voltage modification only, gap size alteration only, and combination of both electrostatic optimization methods.

bit ( $\approx$ 2.5% reduction of the critical vibration amplitude), one can improve the gyroscope angular rate sensitivity almost by a factor of 30.

Note that this figure maps the effects of physical design parameters on the sensitivity, in contrast to figure 2, which maps the effects of the nonlinear coefficients on the sensitivity. Of course, the figures are related through the effects that the design parameters have on the nonlinear coefficients, as described in figures 3, 4(a) and 5(a).

This example clearly illustrates the impact of optimization methods on the dynamic performance of MEMS gyroscopes and provides additional motivation for their further exploration in other types of MEMS resonators.

# 4. Discussion

We have illustrated the ability to modify mechanical and electrostatic contributions to the nonlinear stiffness parameters, both Duffing and mode coupling coefficients, of a thin spinning ring in a systematic manner. Our results suggest that the nonlinear tuning techniques discussed above can be equally applied to ring/disk resonating gyroscopes with more sophisticated geometries, such as those reported in [9, 14]. Importantly, the general expressions for the gyroscope kinetic and potential energies presented in equations (1)–(3) remain the same. However, the functional form of the radial displacement  $u(r,\theta,t)$ , presented in equation (4) for a thin ring, depends on the geometry of the vibrating body. After being calculated numerically using, for example, finite element methods,  $u(r,\theta,t)$  and  $v(r,\theta,t)$  can then be used in equations (1)–(3) in order to compute the linear and nonlinear modal parameters of interest. An example of such a computational analysis for the case of a uniform ring and electrode gap but non-uniform DC bias is presented in [35]. In addition, that study validates, for the case of uniform ring with segmented electrodes, the present approach in which we consider only the lowest-order elliptical modes with their dispersive coupling, and for which we omit any coupling to extraneous modes (translational, rotational, etc). Inclusion of such coupling essentially introduces small noise to the dynamics of the drive/sense modes, especially in the case of light damping.

It is important to mention that while we have successfully demonstrated the applicability of the nonlinear tuning methods using rather simple modifications of  $V_{DC}$ ,  $\Delta$ , and/or h, the analysis remains essentially identical if one would like to account for larger number of electrodes in equation (14) or additional terms (e.g. higher harmonics) in equations (18) and (21), although the additional benefits are expected to be minimal.

From a methodological standpoint, the electrostatic tuning methods discussed in sections 3.1 and 3.2 are independent of the gyroscope geometry. For example, in order to take advantage of the non-uniform distribution of the bias voltage, one still needs at least 16 driving/sensing electrodes around the gyroscope circumference. Furthermore, as follows from equation (3), the functional expressions for the electrostatic contributions to  $\kappa$  and  $\gamma$  depend on the particular form of  $u(R, \theta, t)$ , which is expected to be very similar to the one represented by equation (4). As a result, the dependencies of the electrostatic contributions to  $\kappa$  and  $\gamma$  on variations of the bias voltage and/or electrode gap size described by equations (16a), (16b), (20a) and (20b) are expected to be reasonably accurate for more complex geometries, e.g. DRGs. However, it is important to note that while we have shown that modifications in the electrostatic setup of ring gyroscopes should lead to considerable improvements in the gyroscope sensitivity, the same design changes may have less dramatic effect in gyroscopes with stiffer geometries, such as DRGs, where mechanical contributions to nonlinear coefficients are expected to be larger.

The mechanical tuning method presented in section 3.3, unlike its electrostatic counterparts, strongly depends on the gyroscope geometry. While the ring geometry is essentially defined by two parameters, its midline radius and radial thickness, the dimension of the parameter space for gyroscopes reported in [14, 42] is much higher. In this case, unfortunately, it is no longer possible to perform simple analytical calculations for the linear and/or nonlinear parameters of interest. Instead, one has to employ numerical shape optimization techniques, such as those described in [32], in order to tailor the gyroscope nonlinear dynamic behavior and improve its performance as a rate sensor. The latter approach, however, can take into account a larger number of design parameters and geometric features of the gyroscope body and may yield more substantial results as compared with those obtained for the ring gyroscope. Results from a study of a ring with variable DC bias on the electrodes that compares detailed calculations of nonlinear coefficients and system response obtained using finite element software with results from a two mode model, offers evidence that such approaches hold promise [35].

### 5. Conclusion

In this work we have demonstrated design approaches that allow one to tune nonlinear stiffness parameters of ring/disk resonating gyroscopes in a systematic manner in order to improve their performance as a rate sensor. Two of these methods involve modifications in the gyroscope electrostatic actuation setup and the other deals with geometrical (inertia and mechanical stiffness) modifications of the gyroscope body.

Our main goal was to maximize the intermodal dispersive coupling strength between the drive and sense modes in order to enhance self-induced parametric amplification, which increases the gyroscope rate sensitivity  $S_{\Omega}$  [9], while simultaneously improving linear dynamic range by suppressing the drive mode Duffing nonlinearity. Specifically, we showed that if the gyroscope actuation/sensing scheme has at least 16 electrodes, it becomes possible to modify the intermodal coupling strength and the modal Duffing constant by applying a non-uniform distribution of the bias voltage. Additionally, we demonstrated that a non-uniform electrode gap size also affects the magnitude of the gyroscope nonlinear coefficients and can be used to tailor the gyroscope nonlinear dynamic behavior. Finally, we illustrated the applicability of shape optimization methods in manipulating the nonlinear stiffness parameters of a thin spinning ring by altering the ring radial thickness along the ring circumference. By illustrating these approaches using a thin spinning ring as an example, we have shown that while the last optimization approach yielded relatively small increase of nonlinear coefficients, the electrostatic in combination, can result in more than an order of magnitude improvement of the ring gyroscope sensitivity. Of course, for DRGs and other mechanically stiff resonators, the mechanical effects will be larger and a combined optimization approach will no doubt offer even more benefit.

In the light of these results, future efforts can be focused on (i) experimental implementation of these ideas on a ring resonator and (ii) adapting the tuning methods presented here for application in more general ring/disk geometries in an attempt to improve their angular rate sensitivity. These approaches will likely involve detailed computational approaches such as those described in [32–35].

# Data availability statement

No new data were created or analysed in this study.

# **Acknowledgments**

This work was supported by grants from DARPA (FA8650-13-1-7301), the US Army Research Office (W911NF-12-1-0235), and the National Science Foundation (1561829 and 1662619) and the Binational Science Foundation (2018041). The authors also would like to thank David A Horsley, Sarah Nitzan, and Thomas W Kenny for helpful discussions.

# **Appendix**

In this section we present a system of fully coupled equations of motion derived for a simple ring, [10], rotating with an external angular rate  $\Omega$ . These equations of motion are expressed in terms of the modal coordinates A and B for the drive and sense mode, respectively, and read

$$\ddot{A}\left[1 + \frac{3}{5R^{2}}\left(11A^{2} + B^{2}\right)\right] + \dot{A}\left[2\Gamma_{A} + \frac{6}{5}\frac{B\dot{B}}{R^{2}}\right] + A\omega_{0}^{2}$$

$$+ A\left[\Omega^{2}\left(\frac{11}{5} - \frac{37B^{2}}{10R^{2}}\right) + \kappa\frac{B^{2}}{R^{2}} + \frac{33\dot{A}^{2}}{5R^{2}} + \frac{31\dot{B}^{2}}{5R^{2}} + \frac{34\dot{B}B}{5R^{2}}\right]$$

$$+ \frac{A^{3}}{R^{2}}\left[\gamma - \frac{33}{10}\Omega^{2}\right] - \frac{16\dot{B}}{5R^{2}}\Omega A^{2} = \frac{8}{5}\Omega\dot{B}\left[1 - 2\frac{B^{2}}{R^{2}}\right]$$

$$+ F_{A}(A, B, t), \tag{25}$$

$$\begin{split} \ddot{B} \left[ 1 + \frac{3}{5R^2} \left( 11B^2 + A^2 \right) \right] + \dot{B} \left[ 2\Gamma_B + \frac{6}{5} \frac{A\dot{A}}{R^2} \right] + B\omega_0^2 \\ + B \left[ \Omega^2 \left( \frac{11}{5} - \frac{37A^2}{10R^2} \right) + \kappa \frac{A^2}{R^2} + \frac{33\dot{B}^2}{5R^2} + \frac{31\dot{A}^2}{5R^2} + \frac{34\dot{A}A}{5R^2} \right] \\ + \frac{B^3}{R^2} \left[ \gamma - \frac{33}{10} \Omega^2 \right] - \frac{16\dot{A}}{5R^2} \Omega B^2 = -\frac{8}{5} \Omega \dot{A} \left[ 1 - 2\frac{A^2}{R^2} \right] \\ + F_B(A, B, t), \end{split}$$
(26)

where

$$\omega_0^2 = \frac{1}{5\rho} \left[ 3 \frac{Eh^2}{R^4} - 4 \frac{\epsilon_0 V_{DC}^2}{h\Delta^3} \right],$$

$$\gamma = \kappa = \frac{6R^2}{5\rho} \left[ \frac{Eh^2}{R^6} - \frac{\epsilon_0 V_{DC}^2}{h\Delta^5} \right],$$

$$F_A(A, B, t) = \frac{\epsilon_0 V_{DC} V_{AC}(t)}{5\rho h\Delta^2} \left[ 4 + 3 \frac{B^2}{\Delta^2} + 9 \frac{A^2}{\Delta^2} \right],$$

$$F_B(A, B, t) = \frac{\epsilon_0 V_{DC} V_{AC}(t)}{5\rho h\Delta^4} AB. \tag{27}$$

# **ORCID iD**

Pavel M Polunin https://orcid.org/0000-0001-9810-143X

# References

- [1] Yazdi N, Ayazi F and Najafi K 1998 Proc. IEEE 86 1640-59
- [2] Vig J R 1994 NASA STI/Recon Technical Report N 95 19519
- [3] He Yi and Li Ye 2013 Physical activity recognition utilizing the built-in kinematic sensors of a smartphone *Int. J. Distrib. Sens. Netw.* **9** 481580
- [4] Dang J 2007 Statistical Analysis of the Effectiveness of Electronic Stability Control (ESC) Systems—Final Report HS-810 794 (National Center for Statistics and Analysis) (available at: www-nrd.nhtsa.dot.gov/Pubs/810794.PDF)
- [5] Neul R et al 2007 IEEE Sens. J. 7 302-9
- [6] Barshan B and Durrant-Whyte H F 1995 IEEE Trans. Robot. Autom. 11 328–42

- [7] Luinge H J and Veltink P H 2005 Med. Biol. Eng. Comput. 43 273–82
- [8] Brown T G 2003 Harsh military environments and microelectromechanical (MEMS) devices SENSORS, 2003 IEEE (Toronto, ON, Canada) vol 2 pp 753–60
- [9] Nitzan S H, Zega V, Li M, Ahn C H, Corigliano A, Kenny T W and Horsley D A 2015 Sci. Rep. 5 9036
- [10] Polunin P M and Shaw S W 2017 Int. J. Non-Linear Mech. 94 300–8
- [11] Acar C and Shkel A 2008 Mems Vibratory Gyroscopes: Structural Approaches to Improve Robustness (Berlin: Springer Science & Business Media)
- [12] Remtema T and Lin L 2001 Sens. Actuators A 91 326-32
- [13] Painter C C and Shkel A M 2003 IEEE Sens. J. 3 595-606
- [14] Ahn C H et al 2015 J. Microelectromech. Syst. 24 343-50
- [15] Gallacher B J, Hedley J, Burdess J S, Harris A J, Rickard A and King D O 2005 J. Microelectromech. Syst. 14 221–34
- [16] Kim D J and Closkey R 2006 IEEE Trans. Control Syst. Technol. 14 69–81
- [17] Antonello R, Oboe R, Prandi L and Biganzoli F 2009 *IEEE Trans. Ind. Electron.* **56** 3880–91
- [18] Wong S, Fox C and McWilliam S 2006 *J. Sound Vib.* **293** 266–85
- [19] Ghaffari S et al 2015 J. Microelectromech. Syst. 24 276–88
- [20] Ayazi F and Najafi K 2001 *J. Microelectromech. Syst.* **10** 169–79
- [21] Lee J H, Choi B Y, Park K h and Yoo H J 1998 Vibrating disk type micro-gyroscope US Patent 5,783,749
- [22] Johari H and Ayazi F 2006 Capacitive bulk acoustic wave silicon disk gyroscopes 2006 Int. Electron Devices Meeting, IEDM'06 (San Francisco, CA, USA 11–13 December 2006) (IEEE) pp 1–4
- [23] Kubena R L and Chang D T 2009 Disc resonator gyroscopes US Patent 7.581,443
- [24] Braghin F, Resta F, Leo E and Spinola G 2007 Sens. Actuators A 134 98–108
- [25] Sharma M, Sarraf E H, Baskaran R and Cretu E 2012 Sens. Actuators A 177 79–86
- [26] Oropeza-Ramos L A, Burgner C B and Turner K L 2008 Inherently robust micro gyroscope actuated by parametric resonance *IEEE 21st Int. Conf. on Micro Electro Mechanical Systems*, 2008 (IEEE) pp 872–5

- [27] Oropeza-Ramos L A and Turner K L 2005 Parametric resonance amplification in a MEMGyroscope *IEEE* Sensors, 2005 (IEEE) p 4
- [28] Gallacher B, Burdess J and Harish K 2006 *J. Micromech. Microeng.* **16** 320
- [29] Hu Z, Gallacher B, Burdess J, Fell C and Townsend K 2011 Sens. Actuators A 167 249–60
- [30] Miller N J, Shaw S W, Oropeza-Ramos L A and Turner K L 2008 A MEMS-based rate gyro based on parametric resonance ASME 2008 9th Conf. on Engineering Systems Design and Analysis (American Society of Mechanical Engineers) pp 793–7
- [31] Tatar E, Mukherjee T and Fedder G K 2014 Tuning of nonlinearities and quality factor in a mode-matched gyroscope 2014 IEEE 27th Int. Conf. on Micro Electro Mechanical Systems (MEMS) (IEEE) pp 801–4
- [32] Dou S, Strachan B S, Shaw S W and Jensen J S 2015 Phil. Trans. R. Soc. A 373 20140408
- [33] Dou S 2015 Gradient-based optimization in nonlinear structural dynamics
- [34] Li L L, Polunin P M, Dou S, Shoshani O, Scott Strachan B, Jensen J S, Shaw S W and Turner K L 2017 Appl. Phys. Lett. 110 081902
- [35] Li D, Shaw S W and Polunin P M 2021 J. Struct. Dyn. 1 217–35 (available at: https://popups.uliege.be/2684-6500/index.php?id=96)
- [36] Ahn C, Nitzan S, Ng E, Hong V, Yang Y, Kimbrell T, Horsley D and Kenny T 2014 Appl. Phys. Lett. 105 243504
- [37] Evensen D A 1966 J. Appl. Mech. 33 553-60
- [38] Natsiavas S 1994 Int. J. Non-Linear Mech. 29 31-48
- [39] Shaw S W, Shoshani O and Polunin P M 2017 Modeling for nonlinear vibrational response of mechanical systems *The* Art of Modeling Mechanical Systems (Berlin: Springer) pp 277–319
- [40] Lifshitz R and Cross M 2008 Rev. Nonlinear Dyn. Complexity 1 1–52
- [41] Landau L and Lifshitz E 1959 Classical mechanics
- [42] Senkal D, Askari S, Ahamed M J, Ng E J, Hong V, Yang Y, Ahn C H, Kenny T W and Shkel A M 2014 100K Q-Factor toroidal ring gyroscope implemented in wafer-level epitaxial silicon encapsulation process 2014 IEEE 27th Int. Conf. on Micro Electro Mechanical Systems (MEMS) (IEEE) pp 24–27